THE JOURNAL OF PHYSICAL CHEMISTRY B
A JOURNAL OF THE AMERICAN CHEMICAL SOCIETY

pubs.acs.org/JPCB

Article

Simultaneous Imaging and Characterization of Polyunsaturated Fatty Acids, Carotenoids, and Microcrystalline Guanine in Single *Aurantiochytrium limacinum* Cells with Linear and Nonlinear Raman Microspectroscopy

Published as part of The Journal of Physical Chemistry virtual special issue "Hiro-o Hamaguchi Festschrift".

Risa Sasaki, Shogo Toda, Takaiku Sakamoto, Eiji Sakuradani, and Shinsuke Shigeto*

Cite This: *J. Phys. Chem. B* 2023, 127, 2708–2718

Read Online

ACCESS | Metrics & More | Article Recommendations | Supporting Information

ABSTRACT: Thraustochytrids are heterotrophic marine protists known for their high production capacity of various compounds with health benefits, such as polyunsaturated fatty acids and carotenoids. Although much effort has been focused on developing optimal cultivation methods for efficient microbial production, these high-value compounds and their interrelationships are not well understood at the single-cell level. Here we used spontaneous (linear) Raman and multiplex coherent anti-Stokes Raman scattering (CARS) microspectroscopy to visualize and characterize lipids (e.g., docosahexaenoic acid) and carotenoids (e.g., astaxanthin) accumulated in single living *Aurantiochytrium limacinum* cells. Spontaneous Raman imaging with the help of multivariate curve resolution–alternating least-squares enabled us to make unambiguous assignments of the molecular components we detected and derive their intracellular distributions separately. Near-IR excited CARS imaging yielded the Raman images at least an order of magnitude faster than spontaneous Raman imaging, with suppressed contributions of carotenoids. As the culture time increased from 2 to 5 days, the lipid amount increased by a factor of ∼7, whereas the carotenoid amount did not change significantly. Furthermore, we observed a highly localized component in *A. limacinum* cells. This component was found to be mixed crystals of guanine and other purine derivatives. The present study demonstrates the potential of the linear–nonlinear Raman hybrid approach that allows for accurate molecular identification and fast imaging in a label-free manner to link information derived from single cells with strategies for mass culture of useful thraustochytrids.

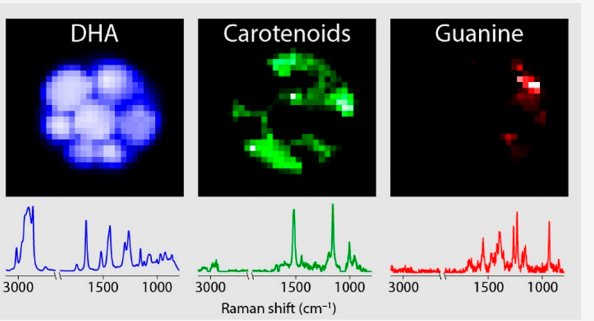

INTRODUCTION

Microbial production offers a sustainable alternative to conventional sources of high-value compounds such as fuel and nutraceuticals. During the past few decades, thraustochytrids, heterotrophic oleaginous microalgae widespread in marine and mangrove areas, have garnered a good deal of attention because they produce high levels of docosahexaenoic acid (DHA).[1] DHA is classified as an omega-3 (ω-3, 22:6) polyunsaturated fatty acid (PUFA) with the first C=C bond located at the third carbon atom from the methyl terminus (Figure 1a). It is essential for the proper development and function of the brain and eye. Furthermore, studies have suggested that DHA is effective in preventing and/or ameliorating diseases such as Alzheimer's disease, arteriosclerosis, and cancer.[2] However, DHA cannot be synthesized *de novo* in mammals and must be obtained from the diet. The current primary source of dietary DHA is fish oil, which suffers from various issues including unstable quality, environmental pollution, unpleasant odor and taste, and catch limits.[3] Microbe-derived oils (often referred to as single-cell oils) have thus been expected as a new natural source that can circumvent these problems and is amenable to scale-up through culture and process optimization.[3,4]

In addition to PUFAs, strains of thraustochytrids are also known to produce other kinds of commercially important compounds: carotenoids and squalene.[1] Carotenoids are yellow to orange-red lipophilic pigments with diverse physiological functions (e.g., photoprotection, antioxidant, and anti-inflammatory) and have found applications not only as colorants but also in dietary supplements and cosmetics.[5,6] Astaxanthin (Figure 1b) is arguably one of the most

Received: January 13, 2023
Revised: March 2, 2023
Published: March 15, 2023

https://doi.org/10.1021/acs.jpcb.3c00302
J. Phys. Chem. B 2023, 127, 2708–2718

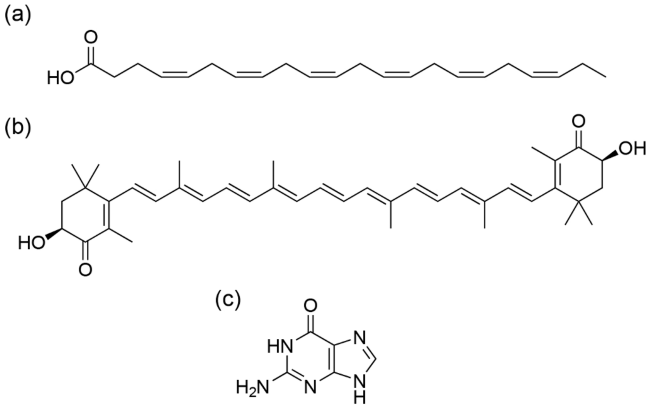

Figure 1. Chemical structures of DHA (a), astaxanthin (b), and guanine (c).

commercially successful carotenoids. Although chemical synthesis is the primary production route for astaxanthin on the market, strong consumer demand for natural products has led to a growing interest in microbial production. Microbial production of astaxanthin typically utilizes the Chlorophyta *Haematococcus*. For example, the potent astaxanthin producer *H. pluvialis* accumulates significant amounts of astaxanthin when cultured under stress conditions, reaching ∼3% of cell dry weight.[5,6] Unlike the synthetic counterpart, *Haematococcus* astaxanthin occurs predominantly as one of three stereoisomers, i.e., the 3*S*,3*S*′ isomer[5,6] (see the configuration of the two hydroxyl groups in Figure 1b). Squalene is another useful substance produced by some thraustochytrids. This triterpene hydrocarbon is widely used in nutraceuticals, cosmetics, and vaccine adjuvants.[7] As with DHA, the commercial supply of squalene largely relies on fish, so alternative sources have been searched for.

To achieve full commercialization of PUFAs and other useful compounds produced by thraustochytrids, the development of efficient production methods and molecular breeding is crucial. Much of the work toward this goal has employed destructive, bulk analysis such as gas chromatography−mass spectrometry (GC−MS), but nondestructive, single-cell analysis is required to understand the cell-to-cell variation, intracellular distributions, and interrelationships of those compounds. Raman microspectroscopy, which uses spontaneous (or linear) Raman scattering, has emerged as a promising optical tool for studies of single living cells. Based on the inelastic scattering of light by molecular vibrations, it provides detailed information about molecules in cells without the need for labels, regardless of the type of molecule or cell. Because lipids (including fatty acids) and carotenoids generate relatively strong Raman signals under typical experimental conditions, microalgae have been the subject of intensive Raman studies.[8] The microalgal species studied so far include *Botryococcus braunii*,[9] *Desmodesmus quadricauda*,[10,11] *Chlorella vulgaris*,[10] *Euglena gracilis*,[12,13] and *H. pluvialis*.[14,15]

A major drawback of Raman microspectroscopy is its inherently weak signal. Raman scattered light is easily buried by the presence of (auto)fluorescence, and a long signal accumulation is generally required to obtain good-quality Raman spectra, making high-speed imaging very difficult. To overcome these difficulties associated with spontaneous Raman scattering, coherent (or nonlinear) Raman microscopy based on nonlinear optical effects has been developed and applied to cells and even larger samples such as tissues.[16] The preponderance of nonlinear Raman spectroscopies utilizes third-order nonlinearities, with coherent anti-Stokes Raman scattering (CARS) and stimulated Raman scattering (SRS) being the most commonly employed.[17] Although many applications of CARS and SRS microscopy to microalgal cells have been reported, most of them have focused only on a specific target component (e.g., lipids[18−20] and paramylon[21]) due to limited spectral information. Simultaneous visualization and quantification of multiple biomolecules of different types are still scarce.[22]

Here, we leveraged both spontaneous Raman and ultrabroadband multiplex CARS microspectroscopy to address this challenge in single living cells of the thraustochytrid *Aurantiochytrium limacinum* SR21 (formerly known as *Schizochytrium limacinum*[23]). This strain can produce lipids that account for about 70% or more of its biomass, of which 30−40% is DHA.[24] We augmented spontaneous Raman microspectroscopy with multivariate curve resolution−alternating least-squares (MCR−ALS) analysis,[25−27] thereby extracting Raman spectra and intracellular distributions of lipids (e.g., DHA) and carotenoids (e.g., astaxanthin) of *A. limacinum* at different culture times from hyperspectral imaging data. Unexpectedly, we detected a highly localized component that exhibits a spectral profile distinctly different from lipids and carotenoids. Owing to the authentic and complete molecular fingerprint imparted by the observed spontaneous Raman spectra, we were able to unambiguously assign this component to biogenic guanine (Figure 1c) microcrystals mixed with other purines.[28] Guanine as a crystalline inclusion in photosynthetic microalgae has already been identified by Mojzeš et al.[11,29] and by Jantschke et al.,[30] but it has not yet been reported for oil-producing thraustochytrids, to our knowledge. Because microcrystalline guanine is present in only a small fraction of *A. limacinum* cells and also at limited intracellular positions, its detection will entail whole-cell imaging for many cells, for which CARS is far superior to the spontaneous Raman method. The present study demonstrates that the linear−nonlinear Raman hybrid approach, though rarely seen in the literature, is powerful for the characterization and screening of microalgal cells with a high capacity to produce high-value compounds even if unknown.

MATERIALS AND METHODS

Chemicals. D-Glucose and guanine (>97.0%) were purchased from FUJIFILM Wako Pure Chemical Corporation. DHA (≥98%) was purchased from Sigma-Aldrich. Agar powder was purchased from Nacalai Tesque. Bacto yeast extract was purchased from Becton, Dickinson and Company. Artificial seawater salt (TetraMarine Salt Pro) was purchased from Spectrum Brands Japan.

Microalgal Culture. The *A. limacinum* SR21 strain was cultured on a GY seawater agar plate containing D-glucose (40 g L^{-1}), yeast extract (15 g L^{-1}), half-strength artificial seawater (500 g L^{-1}), and agar (20 g L^{-1}) at 25 °C for 2 days. A single colony was picked and grown in a test tube with 4 mL of GY seawater medium containing D-glucose (40 g L^{-1}), yeast extract (1 g L^{-1}), and half-strength artificial seawater (500 g L^{-1}) at 25 °C and shaken at 200 rpm for 2 and 5 days. 200 μL of the culture medium was transferred to a glass-bottom dish (Matsunami Glass) for Raman and CARS measurements.

Spontaneous Raman Microspectroscopy. Spontaneous Raman measurements were performed using a laboratory-built

https://doi.org/10.1021/acs.jpcb.3c00302
J. Phys. Chem. B 2023, 127, 2708−2718

confocal Raman microspectrometer with a customized Nikon TE2000-U microscope (see Figure S1 for a schematic of the apparatus), which has been described previously.[31−33] The 632.8 nm output from a He−Ne laser (Thorlabs, HNL210L) was used as the Raman excitation light. The laser beam, whose diameter was magnified by a factor of ∼3, was directed to the inverted microscope using an edge filter and a dichroic mirror. It was tightly focused onto the sample placed on a piezoelectric nanopositioning stage (Mad City Labs, Nano-LP100) with a 100×, NA = 1.45 objective (Nikon, CFI Plan Apo Lambda). The laser power at the sample was adjusted to 3 mW. In Raman imaging experiments, the sample was translated in a raster manner at 0.5 μm intervals using the piezoelectric stage controlled via LabVIEW (National Instruments). Backscattered light was collected with the same objective, and its Stokes Raman component was transmitted through the edge filter. After passing through a confocal optical system consisting of a 100 μm pinhole and two f = 50 mm lenses, the Raman signal was dispersed with a 600 mm^{-1} grating in an imaging spectrograph (SOL Instruments, MS3504i) and detected with a charge-coupled device (CCD) detector (Andor Technology, Newton DU970P-BVF). The spectral resolution was 4 cm^{-1}. The CCD exposure time was set to 60 s for recording high-quality space-resolved Raman spectra and 1 s per point for Raman imaging. The lateral and axial spatial resolution was experimentally evaluated to be 0.43 and 4.4 μm, respectively.

Ultrabroadband Multiplex CARS Microspectroscopy. We developed a multiplex CARS microspectroscopic system using supercontinuum (SC) radiation generated in a photonic crystal fiber (PCF).[34,35] The developed apparatus is schematically shown in Figure 2. A sub-nanosecond microchip laser

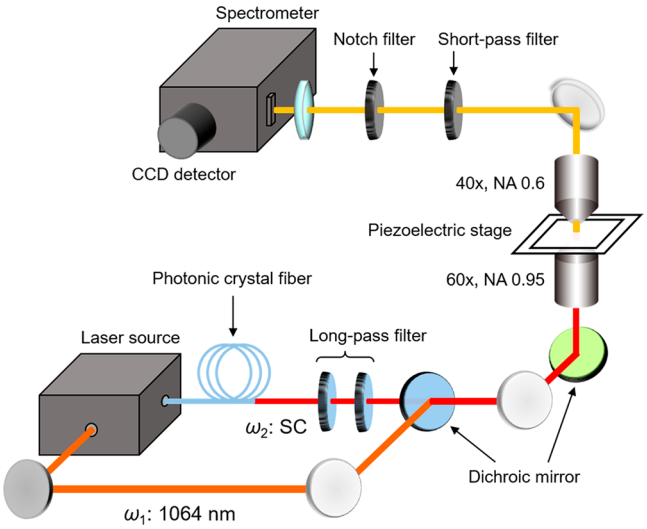

Figure 2. Schematic diagram of the ultrabroadband multiplex CARS microspectroscopic system used in this study. SC, supercontinuum; CCD, charge-coupled device.

(Leukos, OPERA) was used as the main laser source. This laser delivers ∼800 ps pulses centered at 1064 nm at a 33 kHz repetition rate. The laser output was divided into two portions: one was used as the pump (ω_1) beam, and the other was fed to a PCF to generate SC light (typically ranging from 600 to 1800 nm). Only the near-IR portion (1100−1600 nm) of the collimated SC output was selected with long-pass filters and used as the ultrabroadband Stokes (ω_2) beam. This ultrabroadband ω_2 light covers the Raman shift region from 300 to 3150 cm^{-1}. The ω_1 and ω_2 beams were temporally and spatially overlapped and introduced into a customized Nikon ECLIPSE Ti2 microscope. They were focused onto the sample placed on a piezoelectric stage (Mad City Labs, Nano-LP100) with a 60×, NA = 0.95 objective (Nikon, CFI Plan Apo Lambda). The average powers of the ω_1 and ω_2 beams were 9 and 0.9 mW, respectively. As with the above Raman imaging, the sample was raster-scanned at 0.5 μm intervals in CARS imaging. The CARS signal at $\omega_{CARS} = 2\omega_1 - \omega_2$ generated in the forward direction (forward CARS[36]) was collected with a 40×, NA = 0.6 objective (Nikon, CFI S Plan Fluor ELWD). The ω_1 and ω_2 beams propagating with the CARS beam were removed by notch and short-pass filters, respectively. The resulting CARS signal was analyzed with a spectrometer (Teledyne Princeton Instruments, SP2300) and detected with a high-sensitivity CCD detector (Teledyne Princeton Instruments, BLAZE-100HRX). The use of a 600 mm^{-1} grating resulted in a spectral coverage of 720−2200 cm^{-1} and a spectra resolution of 4.4 cm^{-1}. The CCD exposure time was 100 ms per point, 10 times shorter than that employed in Raman imaging experiments. The lateral and axial spatial resolution was determined to be 0.44 and 3.4 μm, respectively.

Spectral Analysis. Unlike spontaneous Raman spectra, as-measured CARS spectra do not represent authentic vibrational spectra due to interference with the nonresonant background. This interference results because the CARS intensity $I(\omega_{CARS})$ is proportional to the square modulus of the third-order optical susceptibility $\chi^{(3)}$ consisting of the vibrationally resonant $\chi_R^{(3)}$ and nonresonant $\chi_{NR}^{(3)}$ terms:

$$I(\omega_{CARS}) \propto |\chi^{(3)}|^2 = |\chi_R^{(3)} + \chi_{NR}^{(3)}|^2 \quad (1)$$

Consequently, CARS spectra often exhibit intricate dispersive profiles (see Figure S2 for an example), which make quantitative analysis difficult particularly when many vibrational resonances overlap, as is often the case with biological Raman spectra. Several numerical approaches such as modified Kramers−Kronig transform methods[37,38] and the maximum entropy method[39,40] (MEM) have been proposed to retrieve the imaginary part (i.e., phase information) of $\chi^{(3)}$, Im[$\chi^{(3)}$]. The Im[$\chi^{(3)}$] spectrum retrieved from the raw CARS spectrum (eq 1) is equivalent to the spontaneous Raman spectrum, and the intensity of a Raman band therein is exactly proportional to the concentration of the molecular species that gives rise to the band. As in previous broadband multiplex CARS studies,[35,40] MEM was adopted here for phase retrieval from the raw CARS spectra divided by the medium spectrum. In the phase retrieval, a fourth-order polynomial was used to estimate a background phase.[40]

In imaging experiments (particularly Raman) on biological samples, it is necessary to use a short exposure time (e.g., 1 s or less) so that scanning is complete in a reasonable time while keeping the laser irradiation as low as possible to avoid photodamage. The imaging data acquired under such conditions are typically accompanied by a large noise, leading to errors in subsequent data analysis such as MCR−ALS, and deterioration of image contrast. Therefore, SVD was used as an effective method for reducing noise without losing or distorting essential vibrational information. Details of the SVD-based denoising employed here can be found in previous publications.[26,41,42] In the present study, ten singular components were retained for the reconstruction of both

https://doi.org/10.1021/acs.jpcb.3c00302
J. Phys. Chem. B 2023, 127, 2708−2718

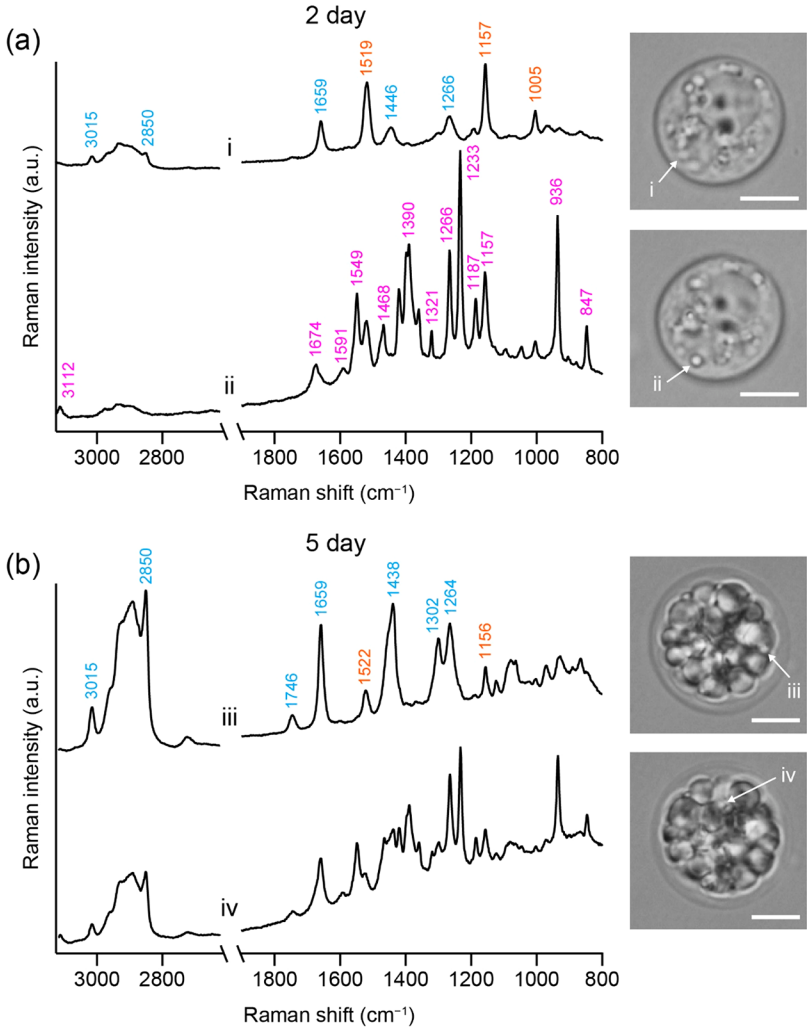

Figure 3. Representative Raman spectra of living *A. limacinum* cells cultured for 2 (a) and 5 (b) days in GY seawater medium (containing 0.1% yeast extract). These spectra were acquired at positions i–iv in four different *A. limacinum* cells whose bright-field images are shown next to the spectra. Scale bar = 5 μm.

Raman and CARS (retrieved Im[$\chi^{(3)}$]) hyperspectral imaging data, by reference to the magnitude of singular values and the spectral pattern of singular vectors.

Univariate Imaging. The most expedient way to generate Raman images in which the spatial distribution of the concentration of a molecular species is visualized from hyperspectral imaging data is to evaluate the intensities of a Raman band attributed to that molecular species and to plot them as a pseudocolor two-dimensional (2D) map.[42,43] Here, this univariate approach was applied to SVD-denoised Raman and Im[$\chi^{(3)}$] spectra. The intensity of the Raman band of interest was obtained by calculating the area intensity between the band contour and a linear baseline that connects the two ends of the interval defining the band.

MCR–ALS. Despite the simplicity, the univariate imaging described above has a limitation in its applicability when multiple molecular components contribute to the same Raman band. Therefore, we also used MCR–ALS, a multivariate feature-extraction technique, to decompose the Raman hyperspectral imaging data into several primary components.[25] In MCR–ALS, an $m \times n$ non-negative matrix **A**, which corresponds to the SVD-denoised Raman hyperspectral imaging data in the present case, is approximated by the product of two low-rank matrices **W** and **H** as

$$\mathbf{A} \approx \mathbf{WH} \tag{2}$$

where **W** is an $m \times k$ matrix whose columns represent the Raman spectra of k components and **H** is a $k \times n$ matrix whose rows represent their spatial concentration profiles. All elements of **W** and **H** are restricted to be non-negative,[44,45] thereby ensuring that **W** and **H** are directly physically interpretable. k represents the number of components that one must assume *a priori*. An appropriate choice of the k value is critical for obtaining a reasonable solution, but it is highly dependent on the nature of the data. No universally applicable criterion has been established.

Because eq 2 is not a unique decomposition unlike SVD, its solution needs to be iteratively optimized to minimize the objective function $\|\mathbf{A} - \mathbf{WH}\|_F^2$, where $\|\cdot\|_F$ denotes the Frobenius norm. There have been many methods for accomplishing this nontrivial task, such as multiplicative update algorithms[45] and gradient descent algorithms, but in this study, the ALS algorithm[44] (non-negative LS) was used. To avoid overfitting and implement the sparsity constraint expected for many kinds of Raman spectra, L_1-norm penalties

https://doi.org/10.1021/acs.jpcb.3c00302
J. Phys. Chem. B 2023, 127, 2708–2718

(also known as lasso[46]) were imposed in the ALS optimization of **W** and **H** as

$$(\mathbf{W}^{\mathrm{T}}\mathbf{W} + \lambda\mathbf{J})\mathbf{H} = \mathbf{W}^{\mathrm{T}}\mathbf{A} \quad (3)$$

$$(\mathbf{H}\mathbf{H}^{\mathrm{T}} + \lambda\mathbf{J})\mathbf{W} = \mathbf{H}\mathbf{A}^{\mathrm{T}} \quad (4)$$

where $\lambda \geq 0$ is the regularization parameter and **J** is an all-ones matrix of dimension $k \times k$. The value of λ was varied on a data-by-data basis. Solving eqs 3 and 4 alternately with the initial matrix of **W** generated from SVD vectors[47] yielded optimal solutions of **W** and **H**. This ALS fitting was repeated 5000 times, which was sufficient for convergence.

SVD noise reduction and calculation of band area in the univariate imaging were performed on Igor Pro 9, whereas MEM and MCR−ALS were performed using in-house code written in Python.

RESULTS

Characterization of Representative Spontaneous Raman Spectra. We began by examining representative spontaneous Raman spectra measured at different positions inside *A. limacinum* cells cultured for 2 and 5 days in GY seawater medium containing 0.1% yeast extract. The Raman spectrum measured at position i (Figure 3a, upper trace) was typical of cells in 2-day culture with pronounced peaks at 1266, 1446, 1659, 2850, and 3015 cm^{-1}. These are well-known Raman bands of unsaturated lipids and are in good agreement with the Raman spectrum of DHA that we measured with the same apparatus (Figure S3) and those reported in the literature.[48−50] The 1266, 1446, and 1659 cm^{-1} bands in the fingerprint region arise from C═C—H bending, CH_2 bending, and *cis*-C═C stretching, respectively.[43] The 2850 cm^{-1} band is attributed to the C—H stretching mode of the CH_2 group, and the 3015 cm^{-1} band, to that of the C═C—H moiety,[49,51] another manifestation of the presence of unsaturated carbon bonds.

The biosynthesis of ω-3 DHA involving a polyketide synthase produces ω-6 PUFA docosapentaenoic acid (DPA; 22:5) as well.[52] Fatty acid compositions in some *A. limacinum* strains determined in previous studies indeed show that DPA is the second most abundant unsaturated fatty acid.[24,53] It is thus likely that DPA also contributes, at least to some extent, to the observed Raman spectra of *A. limacinum* cells.

Other major bands at 1005, 1157, and 1519 cm^{-1} are resonance Raman bands of carotenoids.[54,55] Their mode assignments are as follows: 1005 cm^{-1}, C—CH_3 rocking; 1157 cm^{-1}, C—C stretching; and 1519 cm^{-1}, C═C stretching. The 1005 cm^{-1} band could have a minor contribution from the Raman band associated with the phenylalanine residue of proteins. The Raman spectra of synthetic and microalgal (*H. pluvialis*) astaxanthin are both available in the literature.[14,15] Synthetic, crystalline astaxanthin shows the C═C stretching band at 1512 cm^{-1}, whereas *Haematococcus* astaxanthin shows a slightly up-shifted peak at 1520 cm^{-1}. The latter value agrees well with our observation in *A. limacinum*. This difference in the C═C stretching wavenumber may be accounted for by the fact that it is sensitive to the chemical structure and/or surrounding environment of carotenoids. Astaxanthin most likely exists as esters with fatty acids[6] or is bound to proteins[56] (i.e., carotenoproteins), both of which should shift the C═C stretching band in microalgal cells relative to free astaxanthin.

As is evident from the bright-field images, 5-day cultured cells (Figure 3b) were filled with much larger globules than 2-day cultured cells (Figure 3a). These structures are thought to be lipid droplets composed of fatty acids that the thraustochytrid accumulated during the culture period. The Raman spectrum acquired at position iii (Figure 3b, upper trace) confirms this interpretation: the lipid bands described above became much stronger in intensity than the carotenoid bands at 5 days of incubation. Furthermore, a Raman band at 1746 cm^{-1} is now seen in this spectrum. This band is assignable to the C═O stretching mode of the ester linkage, indicating that DHA (and other PUFAs) was stored in *A. limacinum* cells in the form of triacylglycerols (TAGs).[1,3]

At specific positions such as ii and iv in *A. limacinum* cells at both culture times, we observed Raman spectra (lower traces in Figure 3a,b) that differ substantially from the dominant lipid/carotenoid spectra (upper traces in Figure 3a,b). These spectra have many sharp bands reminiscent of crystalline compounds. A difference spectrum (Figure 4, upper trace)

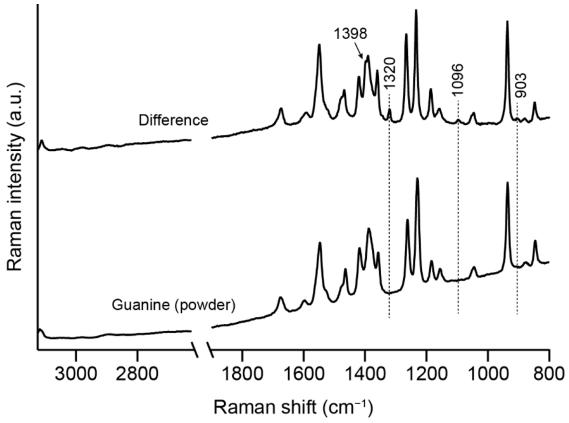

Figure 4. Comparison of the difference spectrum between Raman spectra similar to those measured at positions ii and iv (lower traces in Figure 3a,b) and at positions i and iii (upper traces in Figure 3a,b) and the reference Raman spectrum of a commercial guanine powder.

obtained by appropriately subtracting the contributions of lipids and carotenoids from the aforementioned characteristic spectra is in excellent agreement with the reference Raman spectrum of a commercial guanine powder (Figure 4, lower trace), except for weak bands at 903, 1096, and 1320 cm^{-1} and a shoulder at 1398 cm^{-1}. We can therefore attribute the component giving rise to this characteristic spectral pattern to microcrystalline guanine. This assignment is further corroborated by reference to previous publications reporting the presence of guanine microcrystals in chlorophytes and dinoflagellates.[11,29,30] The origin of the remaining minor bands will be discussed later in this paper.

Univariate Spontaneous Raman Imaging and Quantification of Lipids, Carotenoids, and Guanine. To investigate the intracellular distributions of the lipids (DHA), carotenoids (astaxanthin), and microcrystalline guanine and their quantitative relationships at different culture times, we next performed Raman imaging experiments on ten *A. limacinum* cells cultured for 2 and 5 days. We generated pseudocolor images for the Raman bands of lipids (3015 and 1746 cm^{-1}), carotenoids (1520 and 1005 cm^{-1}), and guanine (936 cm^{-1}). These bands were selected because of their minimal overlap with other bands. Figure 5 displays univariate

https://doi.org/10.1021/acs.jpcb.3c00302
J. Phys. Chem. B 2023, 127, 2708−2718

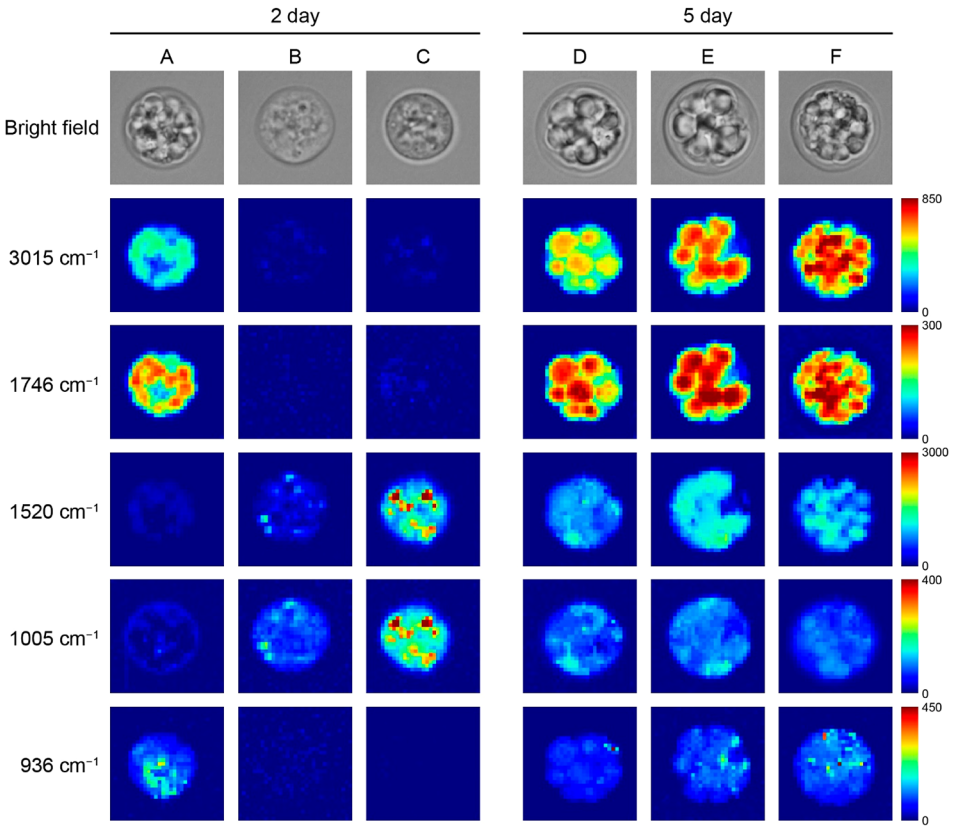

Figure 5. Univariate Raman images at 3015, 1746, 1520, 1005, and 936 cm^{-1} of *A. limacinum* cells cultured for 2 (A−C) and 5 (D−F) days. Also shown are the bright-field images of the cells. The Raman images are displayed in "jet" colormaps. The same color scale applies to all images of each Raman band at both culture times. The spectral window used to calculate the band area was 3002−3027 cm^{-1} for the 3015 cm^{-1} band, 1725−1762 cm^{-1} for the 1746 cm^{-1} band, 1487−1551 cm^{-1} for the 1520 cm^{-1} band, 992−1017 cm^{-1} for the 1005 cm^{-1} band, and 924−949 cm^{-1} for the 936 cm^{-1} band. The image size is 15 × 15 μm^2 (31 × 31 = 961 pixels).

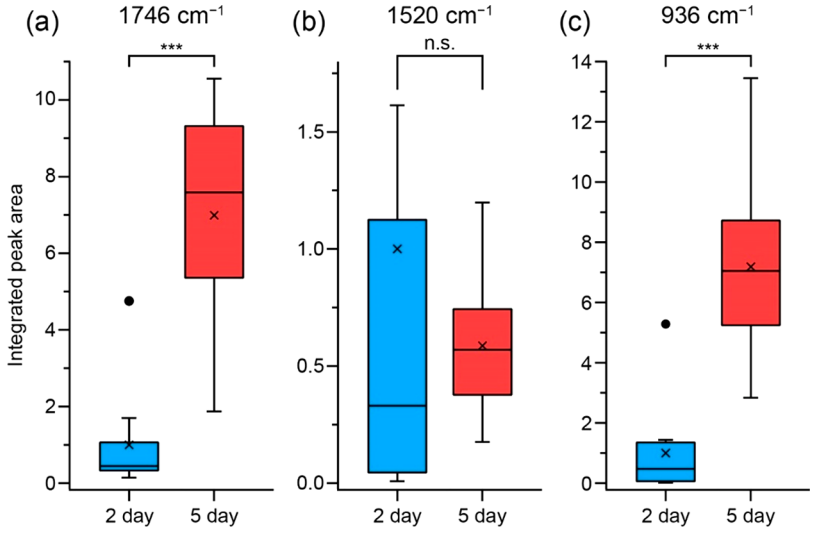

Figure 6. Culture-time dependence of the integrated intensities of the Raman bands at 1746 (a), 1520 (b), and 936 (c) cm^{-1} derived from the univariate Raman images of *A. limacinum* cells (n = 10 for each culture time). The intensities have been normalized to the mean value (represented by the cross symbol within each box) for 2-day culture. Colored boxes show the interquartile range, horizontal lines within the boxes indicate the median, and whiskers span the adjacent values with outliers shown as black dots. ***P < 0.001; n.s., not significant (Welch's t test).

Raman images at these five Raman shifts of three (out of ten) cells for each culture time (cells A−C for 2-day culture and D−F for 5-day culture).

The Raman images of lipids at 3015 and 1746 cm^{-1}, which are nearly identical, indicate that lipids (TAGs) were distributed throughout *A. limacinum* cells and their amount increased from 2 to 5 days of incubation. The carotenoid Raman images at 1520 and 1005 cm^{-1} show a similar trend. The slight difference between the distributions of the 1520 and 1005 cm^{-1} images may be due to the contribution of the

https://doi.org/10.1021/acs.jpcb.3c00302
J. Phys. Chem. B 2023, 127, 2708−2718

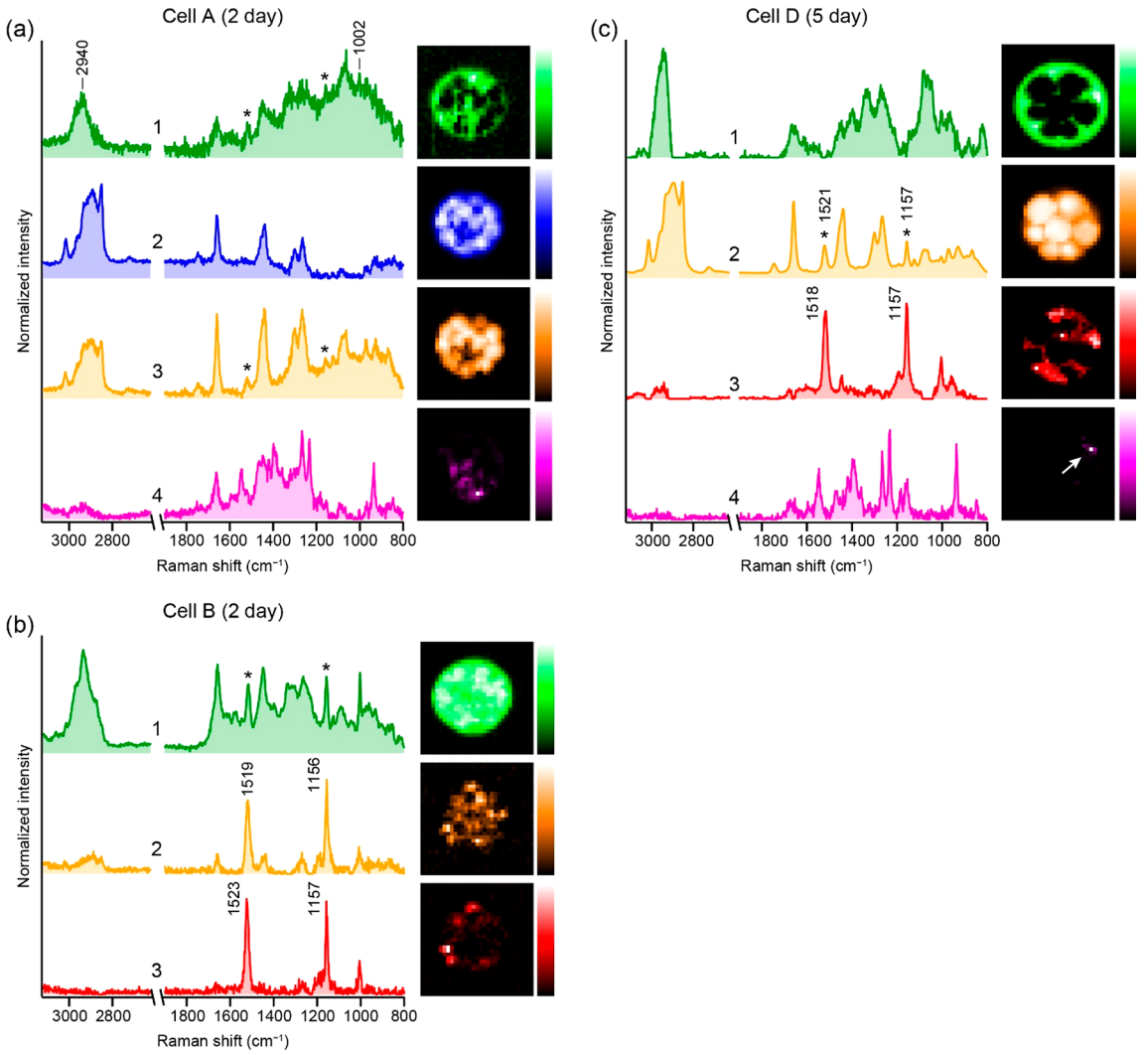

Figure 7. Decomposed spectra (left) and pseudocolor images (right) of the MCR−ALS components for *A. limacinum* cells A (a), B (b), and D (c). The same Raman hyperspectral imaging data as in Figure 5 were analyzed using MCR−ALS with k = 4 (b) and 5 (a, c). One of these components represents the medium, so it is omitted here. The spectra were subjected to vector normalization. Asterisks indicate carotenoid Raman bands.

phenylalanine band at ∼1005 cm^{-1}. As opposed to lipids and carotenoids, the Raman images at 936 cm^{-1} of microcrystalline guanine show highly localized distributions. This result is consistent not only with that obtained by examining the representative Raman spectra (see Figure 3) but also with the features of previously reported Raman images of guanine in other microalgae.[11,29,30]

To quantitatively assess the culture-time dependence of the relative abundances of lipids, carotenoids, and guanine, we summed up the area intensities of the 1746 (lipids), 1520 (carotenoids), and 936 (guanine) cm^{-1} bands over all pixels inside each of the ten *A. limacinum* cells measured (including cells A−F in Figure 5). Figure 6 compares the integrated intensities so determined for the two culture times. The amounts of lipids (Figure 6a) and guanine (Figure 6c) accumulated in the cells in 5-day culture were significantly (P < 0.001) larger than those in 2-day culture. Their mean values in 5-day culture were about 7 times as large as those in 2-day culture. In contrast, the level of carotenoid production and accumulation (Figure 6b) did not differ significantly (P = 0.47) between 2- and 5-day cultures, but the cell-to-cell variation in carotenoid amount appeared to decrease as the culture time increased. We also asked whether there is a correlation between the amounts of these components. As can be seen from Figure S4, none of the 1746 (lipids), 1520 (carotenoids), and 936 (guanine) cm^{-1} bands exhibited a clear correlation with each other at both culture times.

MCR−ALS Raman Imaging Reveals Lipids and Carotenoids with Different Spectral and Spatial Characteristics. To gain more insight into the molecular components in the thraustochytrid, we applied MCR−ALS to the same Raman hyperspectral imaging data as shown in Figure 5. The results of the MCR−ALS analysis (spectra from matrix **W** and images from matrix **H**; see eq 2) are shown in Figure 7 for 2-day cultured cells A and B and 5-day cultured cell D. The number of components, k, was set to 5 for cells A and D and 4 for cell B. In all cases, one of the assumed components represents the medium, so it is omitted in Figure 7. L_1 penalties of λ = 0.001, 0.005, and 0.02 (eqs 3 and 4) were used, respectively, for cells A, B, and D to obtain optimal decomposition results as illustrated below.

Let us first look at the MCR−ALS results of cell A (Figure 7a). As can be seen from Figure 5, this cell is a good example of 2-day cultured cells that accumulated relatively large

https://doi.org/10.1021/acs.jpcb.3c00302
J. Phys. Chem. B 2023, 127, 2708−2718

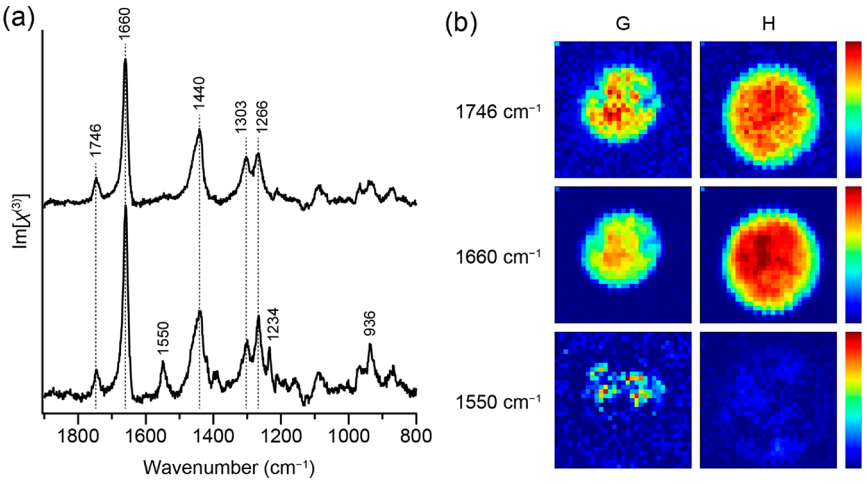

Figure 8. (a) Typical Im[$\chi^{(3)}$] spectra observed in multiplex CARS imaging of single *A. limacinum* cells cultured for 5 days. The upper trace represents a lipid-rich Im[$\chi^{(3)}$] spectrum, whereas the lower trace additionally contains the Raman bands of guanine, as evidenced by the bands at 936, 1234, and 1550 cm^{-1}. (b) Pseudocolor CARS images for two selected cells (denoted G and H), constructed using the area intensities of the 1746 (TAGs), 1660 (unsaturated lipids), and 1550 (guanine) cm^{-1} bands in the Im[$\chi^{(3)}$] spectra. The same color scale applies to the CARS images of each row. The spectral window used to calculate the band area was 1732−1764 cm^{-1} for the 1746 cm^{-1} band, 1639−1709 cm^{-1} for the 1660 cm^{-1} band, and 1537−1567 cm^{-1} for the 1550 cm^{-1} band. The image size is 15 × 15 μm^2 (31 × 31 = 961 pixels).

amounts of lipids. The spectrum of component 1 (Figure 7a, green) exhibits an overall pattern characteristic of proteins with peaks at around 1002, 1250, 1340, 1450, 1656, and 2940 cm^{-1}, which have already been identified in our previous MCR−ALS analysis of fission yeast[25] and filamentous fungal[26] cells. We also see the contribution of carotenoids to component 1 as evidenced by minor bands at ∼1157 and ∼1518 cm^{-1} (indicated by asterisks in Figure 7a). The Raman image of this component displays an inverted distribution of lipid droplets that occupy the central part of the cell. Components 2 (Figure 7a, blue) and 3 (Figure 7a, yellow) are both responsible for lipids. Their spectra are very similar to those in Figure 3b (spectrum iii), and their images coincide with the univariate Raman images at 1746 and 3015 cm^{-1} (Figure 5). The only discernible difference in the spectra of these components is that carotenoid bands are concomitantly observed in component 3. It is clear from the MCR−ALS spectrum and image that component 4 (Figure 7a, magenta) is microcrystalline guanine.

In contrast to cell A, cell B belonged to a subpopulation of *A. limacinum* cells with much lower levels of accumulated lipids and guanine (see Figure 5). Component 1 (Figure 7b, green) is again associated with proteins plus carotenoids (at ∼1157 and ∼1518 cm^{-1}; indicated by asterisks). Components 2 (Figure 7b, yellow) and 3 (Figure 7b, red) show the MCR−ALS spectra dominated by carotenoids, but there are three notable differences between them: the presence/absence of lipid Raman bands; the peak wavenumber of the C═C stretching band of carotenoids (1519 cm^{-1} for component 2 vs 1523 cm^{-1} for component 3); and the localization pattern of the Raman image. These results altogether suggest the presence of two principal carotenoids, a finding that has been derived by virtue of MCR−ALS.

Qualitatively similar results were obtained for cell D, except for guanine (component 4; Figure 7c, magenta). Namely, proteins (component 1; Figure 7c, green) and two types of carotenoids (components 2 and 3; Figure 7c, yellow and red) were identified. As in the case of cell B, the two carotenoid components differ in the intensity of the accompanying lipid bands, C═C stretching wavenumber, and intracellular distribution.

Ultrabroadband Multiplex CARS Imaging. The spontaneous (linear) Raman imaging presented above took as long as 20 min to scan a 15 × 15 μm^2 area containing an *A. limacinum* cell. This image acquisition speed would be insufficient if one is to measure many more cells for screening purposes or to track dynamic changes in a cell. Therefore, we finally attempted ultrabroadband multiplex CARS imaging of *A. limacinum* cells to visualize the intracellular molecules at a faster imaging speed. We randomly selected 15 cells cultured for 5 days in GY seawater medium (containing 0.1% yeast extract) and acquired space-resolved CARS spectra while raster-scanning the sample.

Figure 8a shows typical Im[$\chi^{(3)}$] spectra observed in the CARS imaging experiment. By comparison with the spontaneous Raman results (Figures 3 and 4), we can unequivocally interpret these two spectral patterns as consisting exclusively of lipids (unsaturated, TAGs) and microcrystalline guanine. Note that, in the near-IR excited CARS spectra, the intensities of the carotenoid Raman bands are considerably suppressed compared to those in the visible (i.e., 632.8 nm) excited Raman spectra, despite the preresonance effect.[57,58] Such a disappearance of carotenoid bands may, in general, be considered a disadvantage but could be useful when resonance-enhanced carotenoid bands are so strong that the Raman bands of other compound(s) of interest are obscured.

Figure 8b displays the univariate CARS (Im[$\chi^{(3)}$]) images at 1746 (TAGs), 1660 (unsaturated lipids), and 1550 (microcrystalline guanine) cm^{-1}, constructed for two of the 15 cells (denoted G and H) as examples. CARS images of the other cells can be found in Figure S5. The distributions of the lipid and guanine components mapped in these CARS images are consistent with the corresponding spontaneous Raman images (Figure 5). It is worth noting that, due to the strong nonlinear Raman signal, the CARS images were obtained more than an order of magnitude faster than spontaneous Raman imaging. Because our CARS spectra recorded with a 100 ms exposure time (Figure 8a) are of sufficient quality, it is possible to

https://doi.org/10.1021/acs.jpcb.3c00302
J. Phys. Chem. B 2023, 127, 2708−2718

further reduce the exposure time albeit with some sacrifice of the signal-to-noise ratio.

DISCUSSION

Besides the simultaneous imaging of PUFAs and carotenoids, another significant result of the present study is the characterization of microcrystalline guanine detected in *A. limacinum* cells. Guanine crystals are widely found in the animal kingdom and play unique roles in coloration and visual systems.[59] Despite the biological importance, it was not until recently that the crystal structure of biogenic guanine was determined (usually denoting the β-polymorph).[60] Because of the planar structure and ability to form hydrogen bonds (see Figure 1c), guanine forms a crystal structure in which hydrogen-bonded molecular layers are stacked via $\pi-\pi$ interactions,[59,60] resulting in extraordinary optical properties such as an extremely high refractive index.

The detection of guanine in microalgal cells is not new in itself. Using 532 nm-excited Raman microscopy, Mojzeš and colleagues identified guanine microcrystals as cellular inclusions of photosynthetic autotrophic microalgae such as *D. quadricauda*, *Trachudiscus minutus*, and *Amphidinium carterae* and revealed that microcrystalline guanine serves as an intracellular nitrogen depot.[11,29] Jantschke and colleagues observed in the photosynthetic marine dinoflagellate *Calciodinellum* aff. *operosum* the Raman spectrum of the β-polymorph of anhydrous guanine.[30] They proposed several possible biological roles of the microcrystalline guanine they detected in *C.* aff. *operosum* (e.g., as a light scatterer to increase the efficiency of light utilization by chloroplasts or to protect cells from UV). What is novel about the present study is that microcrystalline guanine was also found in a *non-photosynthetic* microalga (i.e., thraustochytrid). This seems to point to guanine's role in nitrogen storage rather than those related to photosynthesis. A comprehensive study of which genera of marine microorganisms possess microcrystalline guanine will be of great interest in understanding the evolutionary process.

The significance of our results is not limited to proving the universality of microcrystalline guanine in microalgae. As highlighted in Figure 4, we have observed additional Raman features at 903, 1096, 1320, and 1398 cm^{-1} that are absent in the spectra of synthetic guanine powder (Figure 4, lower trace) and the previously reported microalgal cells.[11,29,30] These features had puzzled us, but a very recent paper by Pinsk et al.[28] helped to solve this conundrum. They found that biogenic guanine crystals are not pure crystals but mixed crystals (also known as solid solutions) of guanine and hypoxanthine, a naturally occurring purine derivative. In other words, the structurally similar hypoxanthine is present in the guanine crystal as a dopant without significantly affecting the structure of the host crystal. The Raman spectrum of chemically formed mixed crystals of guanine (β-polymorph) and hypoxanthine given in the Supporting Information of Pinsk et al.[28] does show very weak but distinct Raman features at 1321 and 1399 cm^{-1}, which perfectly agree with our result (Figure 4, upper trace). The other two Raman bands at 903 and 1096 cm^{-1} are not described in that paper probably because they were too weak to be observed with their apparatus.

Ishitsuka et al. investigated *A. mangrovei* cells (strain 18W-13a, a promising squalene producer[61]) using multiplex CARS microspectroscopy and observed spots in some of the *A. mangrovei* cells that are second harmonic generation (SHG)-active.[19] SHG is a second-order nonlinear optical effect and occurs only in systems lacking inversion symmetry. The researchers discussed this SHG-active structure in terms of the cell cycle of *A. mangrovei* as it was detected only in cells cultured for 24 h, but its molecular origin has remained unclear. With our results in mind, we speculate that the SHG spots observed by Ishitsuka et al. in *A. mangrovei* cells could be guanine–hypoxanthine mixed crystals. The SHG activity could arise from the putative non-centrosymmetric structure of the mixed crystal in which hypoxanthine molecules are randomly occluded.[28] We will test this speculation by measuring SHG in *A. limacinum* cells in our future work.

CONCLUDING REMARKS

By taking advantage of MCR–ALS-assisted spontaneous Raman and ultrabroadband multiplex CARS imaging, we have revealed the molecular details, intracellular distributions, and cell-to-cell variation of PUFAs (DHA), carotenoids (astaxanthin), and microcrystalline guanine produced by the thraustochytrid *A. limacinum*. These pieces of information are difficult to obtain with standard techniques such as GC and GC–MS. We have found that the amount of the PUFAs in the form of TAGs markedly increased (about 7-fold) with increasing culture time from 2 to 5 days, whereas that of carotenoids did not change significantly. We have also observed highly localized microcrystalline guanine, which has turned out to occur as mixed crystals with hypoxanthine. This identification has been made possible by the authentic and complete molecular fingerprints in spontaneous Raman spectra. On the other hand, imaging speed also matters, and CARS imaging has enabled us to reduce image acquisition time by a factor of 10 or more. This capability of CARS imaging will be particularly advantageous when visualizing a large number of cells in three dimensions (beyond two dimensions in the present work) to establish the interrelationships between PUFAs, carotenoids, and guanine. The linear–nonlinear Raman hybrid approach holds great promise in these respects.

ASSOCIATED CONTENT

Supporting Information

The Supporting Information is available free of charge at https://pubs.acs.org/doi/10.1021/acs.jpcb.3c00302.

Schematic of the laboratory-built confocal Raman microspectrometer (Figure S1); example of a raw CARS spectrum showing a dispersive shape (Figure S2); comparison of the Raman spectra of *A. limacinum* cells and DHA (Figure S3); scatter plots of the integrated Raman intensities at 1746 cm^{-1} vs 936 cm^{-1}, 1520 cm^{-1} vs 936 cm^{-1}, and 1746 cm^{-1} vs 1520 cm^{-1} for 2- and 5-day cultures (Figure S4); and CARS images at 1746, 1660, and 1550 cm^{-1} of *A. limacinum* cells other than those shown in Figure 8 (Figure S5) (PDF)

AUTHOR INFORMATION

Corresponding Author

Shinsuke Shigeto – *Department of Chemistry, Graduate School of Science and Technology, Kwansei Gakuin University, Sanda, Hyogo 669-1330, Japan;* orcid.org/0000-0002-2035-2068; Email: shigeto@kwansei.ac.jp

https://doi.org/10.1021/acs.jpcb.3c00302
J. Phys. Chem. B 2023, 127, 2708–2718

Authors

Risa Sasaki − *Department of Chemistry, Graduate School of Science and Technology, Kwansei Gakuin University, Sanda, Hyogo 669-1330, Japan*

Shogo Toda − *Department of Chemistry, Graduate School of Science and Technology, Kwansei Gakuin University, Sanda, Hyogo 669-1330, Japan*

Takaiku Sakamoto − *Graduate School of Technology, Industrial and Social Sciences, Tokushima University, Tokushima 770-8513, Japan*

Eiji Sakuradani − *Graduate School of Technology, Industrial and Social Sciences, Tokushima University, Tokushima 770-8513, Japan*

Complete contact information is available at: https://pubs.acs.org/10.1021/acs.jpcb.3c00302

Notes

The authors declare no competing financial interest.

■ ACKNOWLEDGMENTS

This work was supported by the Japan Science and Technology Agency Exploratory Research for Advanced Technology (ERATO) Grant Number JPMJER1502 (S.S.) and the Japan Society for the Promotion of Science KAKENHI Grant Numbers JP19H02821 and JP19H05681 (S.S.).

■ REFERENCES

(1) Aasen, I. M.; Ertesvåg, H.; Heggeset, T. M. B.; Liu, B.; Brautaset, T.; Vadstein, O.; Ellingsen, T. E. Thraustochytrids as Production Organisms for Docosahexaenoic Acid (DHA), Squalene, and Carotenoids. *Appl. Microbiol. Biotechnol.* **2016**, *100*, 4309−4321.

(2) Shahidi, F.; Ambigaipalan, P. Omega-3 Polyunsaturated Fatty Acids and Their Health Benefits. *Annu. Rev. Food Sci. Technol.* **2018**, *9*, 345−381.

(3) Sijtsma, L.; de Swaaf, M. E. Biotechnological Production and Applications of the ω-3 Polyunsaturated Fatty Acid Docosahexaenoic Acid. *Appl. Microbiol. Biotechnol.* **2004**, *64*, 146−153.

(4) Ward, O. P.; Singh, A. Omega-3/6 Fatty Acids: Alternative Sources of Production. *Process Biochem.* **2005**, *40*, 3627−3652.

(5) Guerin, M.; Huntley, M. E.; Olaizola, M. *Haematococcus* Astaxanthin: Applications for Human Health and Nutrition. *Trends Biotechnol.* **2003**, *21*, 210−216.

(6) Lorenz, R. T.; Cysewski, G. R. Commercial Potential for *Haematococcus* Microalgae as a Natural Source of Astaxanthin. *Trends Biotechnol.* **2000**, *18*, 160−167.

(7) Lippi, G.; Targher, G.; Franchini, M. Vaccination, Squalene and Anti-Squalene Antibodies: Facts or Fiction? *Eur. J. Int. Med.* **2010**, *21*, 70−73.

(8) Wei, X.; Jie, D.; Cuello, J. J.; Johnson, D. J.; Qiu, Z.; He, Y. Microalgal Detection by Raman Microspectroscopy. *TrAC Trends Anal. Chem.* **2014**, *53*, 33−40.

(9) Wu, H.; Volponi, J. V.; Oliver, A. E.; Parikh, A. N.; Simmons, B. A.; Singh, S. In Vivo Lipidomics Using Single-Cell Raman Spectroscopy. *Proc. Natl. Acad. Sci. U.S.A.* **2011**, *108*, 3809−3814.

(10) Moudříková, Š.; Mojzeš, P.; Zachleder, V.; Pfaff, C.; Behrendt, D.; Nedbal, L. Raman and Fluorescence Microscopy Sensing Energy-Transducing and Energy-Storing Structures in Microalgae. *Algal Res.* **2016**, *16*, 224−232.

(11) Moudříková, Š.; Nedbal, L.; Solovchenko, A.; Mojzeš, P. Raman Microscopy Shows That Nitrogen-Rich Cellular Inclusions in Microalgae Are Microcrystalline Guanine. *Algal Res.* **2017**, *23*, 216−222.

(12) Ota, N.; Yonamine, Y.; Asai, T.; Yalikun, Y.; Ito, T.; Ozeki, Y.; Hoshino, Y.; Tanaka, Y. Isolating Single *Euglena gracilis* Cells by Glass Microfluidics for Raman Analysis of Paramylon Biogenesis. *Anal. Chem.* **2019**, *91*, 9631−9639.

(13) Iwasaki, K.; Kaneko, A.; Tanaka, Y.; Ishikawa, T.; Noothalapati, H.; Yamamoto, T. Visualizing Wax Ester Fermentation in Single *Euglena gracilis* Cells by Raman Microspectroscopy and Multivariate Curve Resolution Analysis. *Biotechnol. Biofuels* **2019**, *12*, 128.

(14) Kaczor, A.; Baranska, M. Structural Changes of Carotenoid Astaxanthin in a Single Algal Cell Monitored in Situ by Raman Spectroscopy. *Anal. Chem.* **2011**, *83*, 7763−7770.

(15) Kaczor, A.; Turnau, K.; Baranska, M. *In Situ* Raman Imaging of Astaxanthin in a Single Microalgal Cell. *Analyst* **2011**, *136*, 1109−1112.

(16) Kano, H.; Segawa, H.; Leproux, P.; Couderc, V. Linear and Nonlinear Raman Microspectroscopy: History, Instrumentation, and Applications. *Opt. Rev.* **2014**, *21*, 752−761.

(17) Min, W.; Freudiger, C. W.; Lu, S.; Xie, X. S. Coherent Nonlinear Optical Imaging: Beyond Fluorescence Microscopy. *Annu. Rev. Phys. Chem.* **2011**, *62*, 507−30.

(18) Cavonius, L.; Fink, H.; Kiskis, J.; Albers, E.; Undeland, I.; Enejder, A. Imaging of Lipids in Microalgae with Coherent Anti-Stokes Raman Scattering Microscopy. *Plant Physiol.* **2015**, *167*, 603−616.

(19) Ishitsuka, K.; Koide, M.; Yoshida, M.; Segawa, H.; Leproux, P.; Couderc, V.; Watanabe, M. M.; Kano, H. Identification of Intracellular Squalene in Living Algae, *Aurantiochytrium mangrovei* with Hyper-Spectral Coherent Anti-Stokes Raman Microscopy Using a Sub-Nanosecond Supercontinuum Laser Source. *J. Raman Spectrosc.* **2017**, *48*, 8−15.

(20) He, X. N.; Allen, J.; Black, P. N.; Baldacchini, T.; Huang, X.; Huang, H.; Jiang, L.; Lu, Y. F. Coherent Anti-Stokes Raman Scattering and Spontaneous Raman Spectroscopy and Microscopy of Microalgae with Nitrogen Depletion. *Biomed. Opt. Express* **2012**, *3*, 2896−2906.

(21) Wakisaka, Y.; Suzuki, Y.; Iwata, O.; Nakashima, A.; Ito, T.; Hirose, M.; Domon, R.; Sugawara, M.; Tsumura, N.; Watarai, H.; et al. Probing the Metabolic Heterogeneity of Live *Euglena gracilis* with Stimulated Raman Scattering Microscopy. *Nat. Microbiol.* **2016**, *1*, 16124.

(22) Oka, Y.; Yoshida, M.; Minoda, A.; Leproux, P.; Watanabe, M. M.; Kano, H. Label-Free Detection of Polysulfides and Glycogen of *Cyanidium caldarium* Using Ultra-Multiplex Coherent Anti-Stokes Raman Scattering Microspectroscopy. *J. Raman Spectrosc.* **2021**, *52*, 2572−2580.

(23) Yokoyama, R.; Honda, D. Taxonomic Rearrangement of the Genus *Schizochytrium* Sensu Lato Based on Morphology, Chemotaxonomic Characteristics, and 18S rRNA Gene Phylogeny (Thraustochytriaceae, Labyrinthulomycetes): Emendation for *Schizochytrium* and Erection of *Aurantiochytrium* and *Oblongichytrium* gen. nov. *Mycoscience* **2007**, *48*, 199−211.

(24) Huang, T. Y.; Lu, W. C.; Chu, I. M. A Fermentation Strategy for Producing Docosahexaenoic Acid in *Aurantiochytrium limacinum* SR21 and Increasing C22:6 Proportions in Total Fatty Acid. *Bioresour. Technol.* **2012**, *123*, 8−14.

(25) Huang, C.-K.; Ando, M.; Hamaguchi, H.; Shigeto, S. Disentangling Dynamic Changes of Multiple Cellular Components During the Yeast Cell Cycle by *in Vivo* Multivariate Raman Imaging. *Anal. Chem.* **2012**, *84*, 5661−5668.

(26) Yasuda, M.; Takeshita, N.; Shigeto, S. Inhomogeneous Molecular Distributions and Cytochrome Types and Redox States in Fungal Cells Revealed by Raman Hyperspectral Imaging Using Multivariate Curve Resolution−Alternating Least Squares. *Anal. Chem.* **2019**, *91*, 12501−12508.

(27) Hsu, J.-F.; Hsieh, P.-Y.; Hsu, H.-Y.; Shigeto, S. When Cells Divide: Label-Free Multimodal Spectral Imaging for Exploratory Molecular Investigation of Living Cells During Cytokinesis. *Sci. Rep.* **2015**, *5*, 17541.

(28) Pinsk, N.; Wagner, A.; Cohen, L.; Smalley, C. J. H.; Hughes, C. E.; Zhang, G.; Pavan, M. J.; Casati, N.; Jantschke, A.; Goobes, G.; et al. Biogenic Guanine Crystals Are Solid Solutions of Guanine and Other Purine Metabolites. *J. Am. Chem. Soc.* **2022**, *144*, 5180−5189.

(29) Mojzeš, P.; Gao, L.; Ismagulova, T.; Pilátová, J.; Moudříková, Š.; Gorelova, O.; Solovchenko, A.; Nedbal, L.; Salih, A. Guanine, a High-Capacity and Rapid-Turnover Nitrogen Reserve in Microalgal Cells. *Proc. Natl. Acad. Sci. U.S.A.* **2020**, *117*, 32722−32730.
(30) Jantschke, A.; Pinkas, I.; Hirsch, A.; Elad, N.; Schertel, A.; Addadi, L.; Weiner, S. Anhydrous β-Guanine Crystals in a Marine Dinoflagellate: Structure and Suggested Function. *J. Struct. Biol.* **2019**, *207*, 12−20.
(31) Matsuda, A.; Sakaguchi, N.; Shigeto, S. Can Cells Maintain Their Bioactivity in Ionic Liquids? A Novel Single-Cell Assessment by Raman Microspectroscopy. *J. Raman Spectrosc.* **2019**, *50*, 768−777.
(32) Kanno, N.; Kato, S.; Ohkuma, M.; Matsui, M.; Iwasaki, W.; Shigeto, S. Machine Learning-Assisted Single-Cell Raman Fingerprinting for *in Situ* and Nondestructive Classification of Prokaryotes. *iScience* **2021**, *24*, 102975.
(33) Kanno, N.; Kato, S.; Ohkuma, M.; Matsui, M.; Iwasaki, W.; Shigeto, S. Nondestructive Microbial Discrimination Using Single-Cell Raman Spectra and Random Forest Machine Learning Algorithm. *STAR Protoc.* **2022**, *3*, 101812.
(34) Segawa, H.; Okuno, M.; Kano, H.; Leproux, P.; Couderc, V.; Hamaguchi, H. Label-Free Tetra-Modal Molecular Imaging of Living Cells with CARS, SHG, THG and TSFG (Coherent Anti-Stokes Raman Scattering, Second Harmonic Generation, Third Harmonic Generation and Third-Order Sum Frequency Generation). *Opt. Express* **2012**, *20*, 9551−9557.
(35) Kano, H.; Maruyama, T.; Kano, J.; Oka, Y.; Kaneta, D.; Guerenne, T.; Leproux, P.; Couderc, V.; Noguchi, M. Ultra-Multiplex CARS Spectroscopic Imaging with 1-ms Pixel Dwell Time. *OSA Continuum* **2019**, *2*, 1693−1705.
(36) Cheng, J.-X.; Xie, X. S. Coherent Anti-Stokes Raman Scattering Microscopy: Instrumentation, Theory, and Applications. *J. Phys. Chem. B* **2004**, *108*, 827−840.
(37) Liu, Y.; Lee, Y. J.; Cicerone, M. T. Broadband CARS Spectral Phase Retrieval Using a Time-Domain Kramers−Kronig Transform. *Opt. Lett.* **2009**, *34*, 1363−1365.
(38) Masia, F.; Glen, A.; Stephens, P.; Borri, P.; Langbein, W. Quantitative Chemical Imaging and Unsupervised Analysis Using Hyperspectral Coherent Anti-Stokes Raman Scattering Microscopy. *Anal. Chem.* **2013**, *85*, 10820−10828.
(39) Rinia, H. A.; Bonn, M.; Müller, M.; Vartiainen, E. M. Quantitative CARS Spectroscopy Using the Maximum Entropy Method: The Main Lipid Phase Transition. *ChemPhysChem* **2007**, *8*, 279−287.
(40) Vartiainen, E. M.; Rinia, H. A.; Müller, M.; Bonn, M. Direct Extraction of Raman Line-Shapes from Congested CARS Spectra. *Opt. Express* **2006**, *14*, 3622−3630.
(41) Uzunbajakava, N.; Lenferink, A.; Kraan, Y.; Volokhina, E.; Vrensen, G.; Greve, J.; Otto, C. Nonresonant Confocal Raman Imaging of DNA and Protein Distribution in Apoptotic Cells. *Biophys. J.* **2003**, *84*, 3968−81.
(42) Huang, C.-K.; Hamaguchi, H.; Shigeto, S. *In Vivo* Multimode Raman Imaging Reveals Concerted Molecular Composition and Distribution Changes During Yeast Cell Cycle. *Chem. Commun.* **2011**, *47*, 9423−9425.
(43) Huang, Y.-S.; Karashima, T.; Yamamoto, M.; Hamaguchi, H. Molecular-Level Investigation of the Structure, Transformation, and Bioactivity of Single Living Fission Yeast Cells by Time- and Space-Resolved Raman Spectroscopy. *Biochemistry* **2005**, *44*, 10009−10019.
(44) Paatero, P.; Tapper, U. Positive Matrix Factorization: A Non-Negative Factor Model with Optimal Utilization of Error Estimates of Data Values. *Environmetrics* **1994**, *5*, 111−126.
(45) Lee, D. D.; Seung, H. S. Learning the Parts of Objects by Non-Negative Matrix Factorization. *Nature* **1999**, *401*, 788−791.
(46) Tibshirani, R. Regression Shrinkage and Selection Via the Lasso. *J. R. Statist. Soc. B* **1996**, *58*, 267−288.
(47) Boutsidis, C.; Gallopoulos, E. SVD Based Initialization: A Head Start for Nonnegative Matrix Factorization. *Pattern Recognit.* **2008**, *41*, 1350−1362.
(48) Brozek-Pluska, B.; Musial, J.; Kordek, R.; Bailo, E.; Dieing, T.; Abramczyk, H. Raman Spectroscopy and Imaging: Applications in Human Breast Cancer Diagnosis. *Analyst* **2012**, *137*, 3773−3780.
(49) Majzner, K.; Tott, S.; Roussille, L.; Deckert, V.; Chlopicki, S.; Baranska, M. Uptake of Fatty Acids by a Single Endothelial Cell Investigated by Raman Spectroscopy Supported by AFM. *Analyst* **2018**, *143*, 970−980.
(50) Iwasaki, K.; Araki, A.; Krishna, C. M.; Maruyama, R.; Yamamoto, T.; Noothalapati, H. Identification of Molecular Basis for Objective Discrimination of Breast Cancer Cells (MCF-7) from Normal Human Mammary Epithelial Cells by Raman Microspectroscopy and Multivariate Curve Resolution Analysis. *Int. J. Mol. Sci.* **2021**, *22*, 800.
(51) Czamara, K.; Majzner, K.; Pacia, M. Z.; Kochan, K.; Kaczor, A.; Baranska, M. Raman Spectroscopy of Lipids: A Review. *J. Raman Spectrosc.* **2015**, *46*, 4−20.
(52) Ratledge, C. Fatty Acid Biosynthesis in Microorganisms Being Used for Single Cell Oil Production. *Biochimie* **2004**, *86*, 807−815.
(53) Nagano, N.; Taoka, Y.; Honda, D.; Hayashi, M. Optimization of Culture Conditions for Growth and Docosahexaenoic Acid Production by a Marine Thraustochytrid, *Aurantiochytrium limacinum* mh0186. *J. Oleo Sci.* **2009**, *58*, 623−628.
(54) Zheng, Y.-T.; Toyofuku, M.; Nomura, N.; Shigeto, S. Correlation of Carotenoid Accumulation with Aggregation and Biofilm Development in *Rhodococcus* sp. SD-74. *Anal. Chem.* **2013**, *85*, 7295−7301.
(55) Horiue, H.; Sasaki, M.; Yoshikawa, Y.; Toyofuku, M.; Shigeto, S. Raman Spectroscopic Signatures of Carotenoids and Polyenes Enable Label-Free Visualization of Microbial Distributions within Pink Biofilms. *Sci. Rep.* **2020**, *10*, 7704.
(56) Britton, G.; Weesie, R. J.; Askin, D.; Warburton, J. D.; Gallardo-Guerrero, L.; Jansen, F. J.; Groot, H. J. M. d.; Lugtenburg, J.; Cornard, J.-P.; Merlin, J.-C. Carotenoid Blues: Structural Studies on Carotenoproteins. *Pure Appl. Chem.* **1997**, *69*, 2075−2084.
(57) Ozaki, Y.; Cho, R.; Ikegaya, K.; Muraishi, S.; Kawauchi, K. Potential of near-Infrared Fourier Transform Raman Spectroscopy in Food Analysis. *Appl. Spectrosc.* **1992**, *46*, 1503−1507.
(58) Schulz, H.; Baranska, M.; Baranski, R. Potential of NIR-FT-Raman Spectroscopy in Natural Carotenoid Analysis. *Biopolymers* **2005**, *77*, 212−221.
(59) Gur, D.; Palmer, B. A.; Weiner, S.; Addadi, L. Light Manipulation by Guanine Crystals in Organisms: Biogenic Scatterers, Mirrors, Multilayer Reflectors and Photonic Crystals. *Adv. Funct. Mater.* **2017**, *27*, 1603514.
(60) Hirsch, A.; Gur, D.; Polishchuk, I.; Levy, D.; Pokroy, B.; Cruz-Cabeza, A. J.; Addadi, L.; Kronik, L.; Leiserowitz, L. "Guanigma": The Revised Structure of Biogenic Anhydrous Guanine. *Chem. Mater.* **2015**, *27*, 8289−8297.
(61) Kaya, K.; Nakazawa, A.; Matsuura, H.; Honda, D.; Inouye, I.; Watanabe, M. M. Thraustochytrid *Aurantiochytrium* sp. 18W-13a Accummulates High Amounts of Squalene. *Biosc. Biotechnol. Biochem.* **2011**, *75*, 2246−2248.

https://doi.org/10.1021/acs.jpcb.3c00302
J. Phys. Chem. B 2023, 127, 2708−2718